Biotelemetry and Wireless Powering of Biomedical Implants Using a Rectifier Integrated Self-Diplexing Implantable Antenna

Amjad Iqbal, *Graduate Student Member, IEEE*, Muath Al-Hasan, *Senior Member, IEEE*,
Ismail Ben Mabrouk, *Senior Member, IEEE*, Abdul Basir, *Graduate Student Member, IEEE*,
Mourad Nedil, *Senior Member, IEEE*, and Hyoungsuk Yoo, *Senior Member, IEEE*

Abstract—This article proposes an efficient and complete wireless power transfer (WPT) system (WPTS) for multipurpose biomedical implants. The WPTS is composed of a self-diplexing implantable antenna, efficient rectifier, and WPT transmitter (WPT Tx). The proposed system is capable of simultaneously transmitting recorded data and recharging the batteries of the devices (so as to elongate the implant life). The WPT Tx occupies dimensions of $50 \times 50 \times 1.6$ mm^3 and is optimized to effectively transfer power at 1470 MHz to a 55-mm deep implantable device. An efficient and compact (3.4×6.7 mm^2) rectifier is used at 1470 MHz to convert the harvested RF power into a useful direct current (dc) power. The proposed rectifier circuit exhibits a high conversion efficiency of 50% even at an input power of -14 dBm and maximum efficiency of 76.1% at 2 dBm. The proposed self-diplexing implantable antenna occupies small dimensions (9.4 mm^3) and operates at 915 and 1470 MHz by exciting ports 1 and 2, respectively. The biotelemetry operation is performed using a 915 MHz band (port 1), and the rectifier circuit is connected to port 2 (1470 MHz) to perform wireless powering. The simulated results are validated by examining the individual elements (WPT Tx, rectifier, and self-diplexing antenna) and overall WPTS in a saline solution and minced pork. The results prove that the proposed scheme is suitable for biotelemetry and wireless powering of biomedical implants.

Index Terms—Biotelemetry, energy harvesting, implantable antenna, medical implants, rectifier, wide input power range, wireless power transfer (WPT).

Amjad Iqbal and Ismail Ben Mabrouk are with the Department of Engineering, Durham University, Durham DH1 3LE, U.K. (e-mail: amjad730@gmail.com; ismail.benmabrouk@durham.ac.uk).

Muath Al-Hasan is with the Network and Communications Engineering Department, Al Ain University, Al Ain, United Arab Emirates (e-mail: muath.alhasan@aau.ac.ae).

Abdul Basir and Hyoungsuk Yoo are with the Department of Electronics Engineering, Hanyang University, Seoul 04763, South Korea (e-mail: hsyoo@hanyang.ac.kr).

Mourad Nedil is with the Communications Research Laboratory (LRTCS), University of Quebec at Abitibi-Temiscamingue (UQAT), Val-d'Or, QC J9P 1Y3, Canada (e-mail: mourad.nedil@uqat.ca).

I. Introduction

IMPLANTABLE medical devices (IMDs) have emerged as an important part of biomedical engineering due to their ability to monitor and treat impaired organs [1]. Modern IMDs are mostly used in applications such as intracranial pressure monitoring [2], intraoral tongue-drive systems [3], cardiac pacemakers [4], [5], glucose monitoring [6], and wireless capsule endoscopy [7]. IMDs are made to receive and transmit biosignals from the impaired or underinvestigated parts of the body. In fact, IMDs consist of different types of electronics (batteries, sensors, and printed circuit board (PCB) with surface-mounted devices (SMDs), and microcameras) and RF components (rectifier and antenna). Conventionally, electrochemical energy sources (batteries) and direct current (dc) power supply through wires have been common sources for power supply to IMDs [8]. The operational lifespan and size of an IMD are completely dependent on the battery; nevertheless, battery usage increases the temperature and overall dimensions of the IMD, and patients must undergo undesired surgeries to replace dead batteries [9]. As a result, driving IMDs with dc wires may cause infection aches and pain in the impaired organ [10]. To overcome these drawbacks, wireless power transfer (WPT) has been recently recommended for seamlessly and safely driving IMDs [11], [12].

In this area, WPT is considered as a remarkable approach to charge and drive electronic components for a wide range of applications, including those in biomedical engineering [13]. For example, the charging and driving of electronic components in IMDs [14] and automobile batteries [15] via magnetic resonance are studied in [16] and [17]. Other techniques, such as near-field inductive coupling [18], [19] and capacitive coupling [20], have also been used to drive electronic components of IMDs. These techniques have been adopted in spinal cord stimulators (SCSs), prosthetics, and cochlear implants. However, several issues are associated with these techniques, such as a small transfer distance, large receiver (Rx) coils, and power leakages. Furthermore, the power transfer efficiencies (PTEs) of these techniques depend on the sizes of the transmitter (Tx) and Rx coils, and the separation and misalignments between them. Recently, a multicoil Tx is designed to address the misalignments between the Tx and
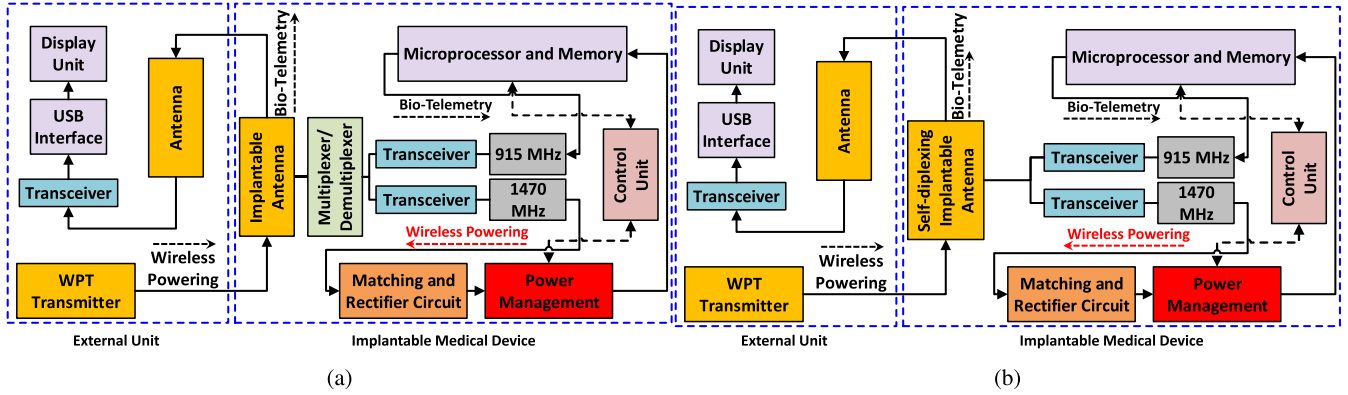
Fig. 1. Generalized block diagram of (a) WPT system with conventional dual-band antenna and (b) WPT system with proposed self-diplexing antenna.

Rx coils [21], [22]. In addition, WPT techniques include the transmission of electromagnetic (EM) free-space radiation, and midfield WPT for driving IMDs deep inside organs is also studied [9]. The advantages of EM wave propagation for WPT include an extensive distance coverage inside human tissue. However, conventional field sources, such as antennas, cannot provide suitable patterns for WPT, as they lack control over the phase. Hence, patterned patches can initiate directed-fields by controlling their phases [23], [24]. Chow *et al.* [24] magnified the PTE of a midfield WPT by patterning EM fields inside the human body.

A high-performance implantable antenna plays a significant role in data transmission. These implantable antennas are often integrated with a rectifier to drive the electronic components of IMDs. Several studies have been reported on implantable antennas for different applications [2], [7]. In [25], a rectifier-integrated quad-band implantable antenna is designed for multitasking biomedical implants; one frequency band is devoted to energy harvesting, and the rest are used for data transmission and wakeup signaling. In [26], a WPT system is presented for scalp-implantable devices. It uses a dual-band antenna, WPT Tx, and rectifier. One band (915 MHz) of the antenna is used for biotelemetry and the other (1900 MHz) for wireless powering. In [27], a dual-band implantable antenna is introduced for wireless powering and wireless data telemetry; the antenna and rectifier share a common ground. A dual-band implantable rectenna is reported in [28] for far-field WPT. The simulated RF-dc conversion efficiency of 42% is obtained for an input power of −10 dBm. The antennas mentioned above are useful for multiband or wideband operations. However, all of them either transmit or receive data in all bands simultaneously, where an external multiplexer is required for independent transmission and reception in all bands through a single antenna. It is obvious that the same antenna cannot operate in dual-mode (as a transmitting antenna for data transmission and as a receiving antenna for wireless powering). Therefore, a highly isolated multiplexer circuit is required for dual-mode operation. However, biomedical implants have minimal space, and an additional multiplexer circuit increases the complexity and size of the IMDs. Moreover, an additional multiplexer circuit consumes power, which affects the overall performance

TABLE I
GENERAL COMPARISON OF THE CONVENTIONAL
AND PROPOSED WPT SYSTEMS

Parameter	Conventional WPT System	Proposed WPT System
Is external multiplexer required for dual-mode operation?	Yes	No
Power consumption	High	Low
Complexity	High	Low
End-to-end transmission efficiency	Low	High
Size of IMD	Large	Small

(transmission efficiency and battery life) of the IMDs. Furthermore, managing different power levels at different bands through one antenna is very difficult. When the WPT and data telemetry bands are closer, the WPT suppresses the telemetry band due to the receiving WPT power, which is much higher than the transmission power of the implant [25]. To address these issues, we introduced the concept of self-diplexing to maintain compactness [29], [30] and to be operated in dual modes (transmission and reception) simultaneously. Moreover, there is no external circuitry (multiplexer circuit) required in the self-multiplexing antennas. Therefore, compactness is ensured. A generalized comparison of the proposed WPT system with conventional WPT systems is illustrated in Table I. The introduction of the self-diplexing approach (proposed WPT system) has a significant impact on the whole IMD system. It simplifies the overall structure and functionality of IMDs, reduces the size of circuitry and extra-power consumption, enhances the end-to-end transmission efficiency of the system, and enhances the power transfer efficiency (compared to [25]) by 2 dB (almost 37% improvement) due to high isolation of telemetric and WPT ports.

The key issues in IMDs consist of real-time multitasking, system complexity due to external multiplexers, power consumption by the extra components of the device, and suppression of adjacent bands in multiband biomedical implants. To alleviate these issues, in this study, we introduced a concept of self-diplexing antenna for the simultaneous biotelemetry and wireless powering of biomedical implants. The complete
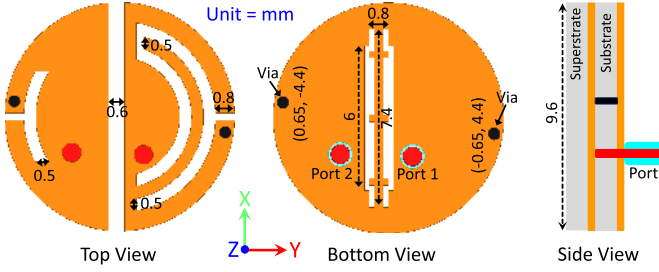
Fig. 2. Top, bottom, and side views of the proposed antenna (unit = mm).

WPT system consists of a WPT Tx and a rectifier-integrated self-diplexing antenna, in which each of the two highly isolated ports is assigned to a unique task. Initially, the WPT Tx is designed at 1470 MHz, followed by a rectifier design at the same frequency. The self-diplexing implantable antenna (operating at 915 and 1470 MHz) is designed with one port connected to a rectifier circuit, to convert the RF energy to useful dc energy from the WPT at 1470 MHz. The second port is connected to a Tx network to transfer the useful information from the impaired organs to an on-body or far-away outside receiver at 915 MHz. The main contributions of the proposed work can be summarized as follows.

1) To the best of our knowledge, this is the first-ever contribution that introduces the self-diplexing antenna with an efficient system solution for both biotelemetry and wireless powering in biomedical implants. The proposed system does not require an additional multiplexing circuit for the dual-mode operation, as shown in Fig. 1.
2) The proposed rectifier circuit exhibits a high conversion efficiency (50% efficiency at a low input power of −14 dBm and a peak efficiency of 76.1% at 2 dBm).
3) The receiving and transmitting channels have isolation of better than 21 dB, despite a compact design with an edge-to-edge distance of $0.0038\lambda_{g1}$ (where λ_{g1} is the guided wavelength at the lower-frequency band).

II. DESIGN METHODOLOGY

A. Self-Diplexing Antenna Design

The layout (top, bottom, and side views) of the proposed self-diplexing antenna is illustrated in Fig. 2. The proposed self-diplexing antenna consists of two semicircular patches with a common ground plane. Each radiating patch is loaded with a shorting pin, open-ended rectangular slot, and arc-shaped slot for operating the structure below its dominant resonant mode. A patterned slot is loaded in the ground plane to reduce the associated coupling between resonators. Both radiators are closely placed with an edge-to-edge distance of $0.0038\lambda_{g1}$ (where λ_{g1} is the guided wavelength at the lower frequency band). Both radiating patches are excited with a 50-Ω coaxial cable. A thin (0.13 mm) and high-dielectric ($\epsilon_r = 10.2$) material, i.e., Rogers RO 3010 (tan $\delta = 0.0022$), is used as a substrate and superstrate. The detailed design procedure is presented in Section. II-A1.

1) Design Evolution: The design and optimization process of the proposed antenna is shown in Fig. 3(a). The corresponding reflections (S_{11} and S_{22}) and transmission coefficients (S_{21})
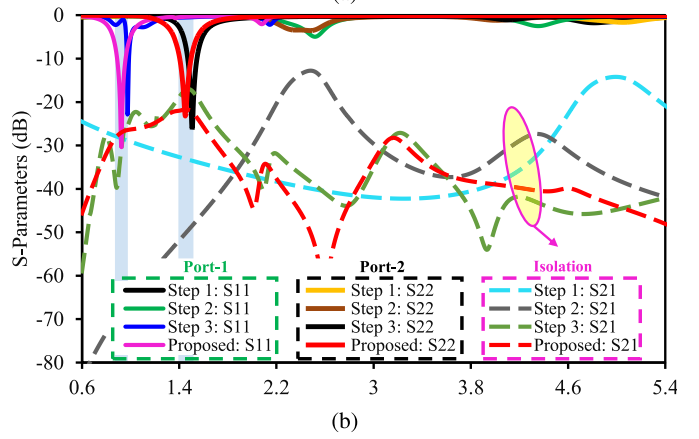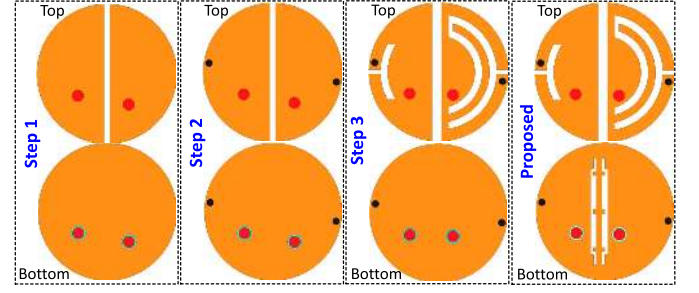

(a)

(b)

Fig. 3. Design and optimization process of the antenna (a) design evolution steps and (b) corresponding s-parameters.

are plotted in Fig. 3(b). The initial dimensions of the circular patch were calculated using the following:

$$f_{\text{res}} = \frac{1.8412 \times c}{4\pi R_p \sqrt{\epsilon_r}}. \tag{1}$$

In the above, f_{res} is the resonant frequency of the circular radiating patch, ϵ_r is the substrate relative permittivity (10.2), R_p is the radius of the circular patch, c is the speed of light (with a numerical value of 3×10^8 m/s), and h is the thickness of the substrate.

The circular patch was further centrally divided into two semicircles separated by a 0.6-mm gap, and the semicircular patches were excited asymmetrically using a 50-Ω coaxial probe. It can be seen that the antennas in the initial step (Step 1) resonated at approximately 5 GHz, with the isolation of 12.3 dB; however, they were not well matched. In Step 2, shorting pins were placed at the edge of each radiator to shift the operating bands toward the lower frequencies. As a result, the antennas resonated at nearly 2.5 GHz, with the isolation of 14.8 dB. Notably, the resonant frequency was shifted from 5 to 2.5 GHz, thereby achieving 50% miniaturization by loading the shorting pins. Furthermore, in Step 3, centrally opened arc slots were etched on the radiating patches, so as to match the antenna and shift the resonant frequencies to lower frequencies. In fact, the slots on the patches elongated the current paths, resulting in antenna resonances at 935 and 1500 MHz (with adequate matching), respectively. The radiating slots induce an additional capacitance effect; thus, the resonant frequency shifted to the lower frequencies [31]. The impact of the additional capacitance on the resonant frequency
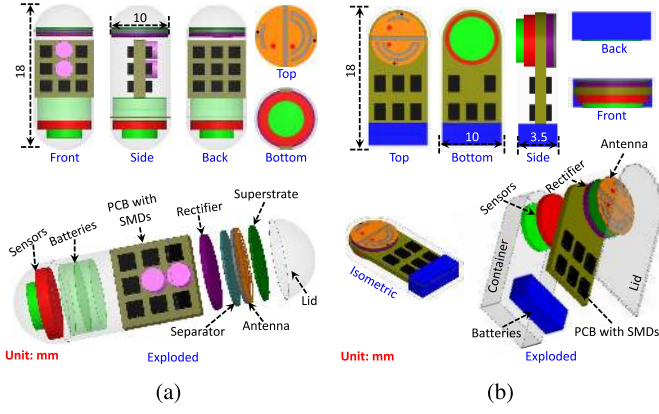
Fig. 4. System architecture (a) capsule-type device for deep tissue implantation and (b) flat-type device for skin implantation.

Fig. 5. (a) Simulation setup and (b) fabricated prototype and measurement setup.

of the antennas can be understood based on the slow wave phenomenon [32]. A combination of a series inductance ($L_\circ$) and capacitance ($C_\circ$) represents an equivalent circuit of the antenna, similar to an ideal transmission line [32]. Equation (2) shows the relationship between the propagation velocity and reactance (inductance and capacitance) of the antenna. It can be observed that the propagation velocity is inversely proportional to the reactance. The arc-shaped and rectangular slots induced a capacitance effect, thus increasing the capacitance value in (2). Therefore, the propagation velocity is reduced, and a lower resonant frequency is achieved when the guided wavelength is constant

$$v_p = \frac{1}{\sqrt{L_\circ C_\circ}} = \frac{c}{\sqrt{\epsilon_{\text{eff}}}} = \lambda_g f_{\text{res}}. \tag{2}$$

Here, v_p is the propagation velocity, $L_\circ$ is the total inductance, $C_\circ$ is the total capacitance, c is the speed of light in vacuum, λ_g is the guided wavelength, and f_{res} is the resonant frequency.

To further move the resonance to the desired lower bands and improve the isolation, the ground plane was modified by adding a symmetric patterned slot, as shown in Step 4. The antenna resonated at 915 MHz with a 10-dB bandwidth of 90 MHz (870–960 MHz) when port 1 was excited. Similarly, the antenna resonated at 1470 MHz with a 10-dB bandwidth of 108 MHz (1402–1510 MHz) when port 2 was excited. In addition, the isolation of the resonators was better than 21 dB. In summary, in the optimization process, the antenna resonant frequency was shifted from 5 GHz to 915 MHz by introducing shorting pins and open-ended rectangular and arc-shaped slots. In addition, the isolation was enhanced from 16 to 21 dB by modifying the ground plane. The higher isolation between the ports makes it a self-diplexing antenna, as shown in Fig. 3(b).

2) System Architectures (Flat- and Capsule-Type Implantable Devices): Every IMD has a particular implantation area and device architecture [4]. All types of electronic and RF components are embedded in IMDs, such as cameras, batteries, sensors, PCBs, and RF components, such as antennas, filters, and rectifiers. In system-level studies, most of the research works have only reported on capsule- or
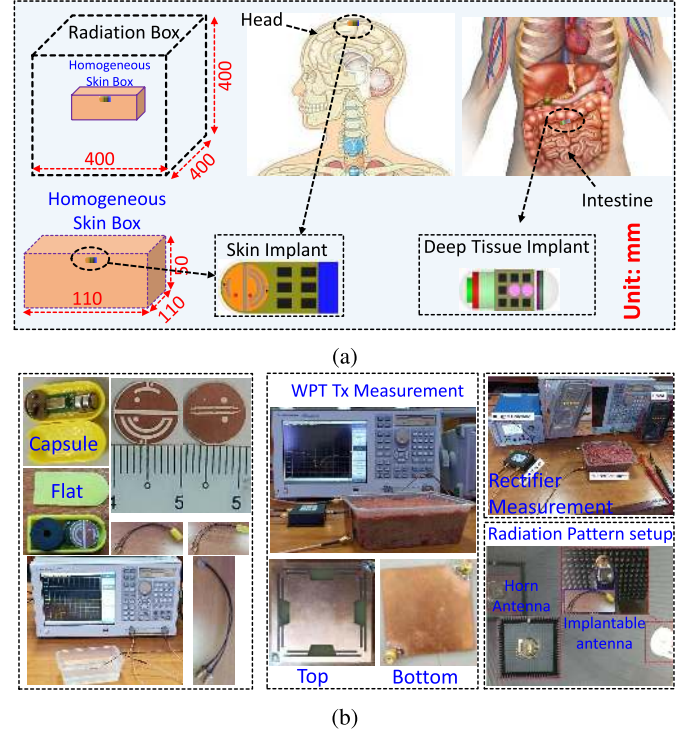
flat-type devices. However, in this work, both architectures are considered and studied. The system architectures of the capsule-type (deep tissue implantation) and flat-type (skin implantation) devices are shown in Fig. 4(a) and (b), respectively. The capsule-type device is extensively used for deep tissue implantation, such as capsule endoscopes and leadless pacemakers, whereas the flat-type devices are used for skin implantation, such as SCSs and deep brain stimulators (DBSs). In this study, the capsule-type device has overall dimensions of $5^2 \times \pi \times 18$ mm^3, and the flat-type device has overall dimensions of $10 \times 18 \times 3.5$ mm^3. Each (capsule-type and flat-type) IMD consists of an antenna, rectifier, batteries, sensors, and a PCB. Capacitors, inductors, and resistors with various values were placed on the PCB during the simulation. A 0.1-mm-thick biocompatible material ($\epsilon_r = 9.8$ and $\tan \delta = 0.006$) was used as a casing for both IMDs. The containers of both devices were tightly closed with epoxy to avoid liquid entering during the practical measurements.

3) Simulation Environments and Measurement Setups: A one-layer homogeneous skin model with dimensions of $110 \times 110 \times 50$ mm^3 was chosen for simulating the proposed antenna in a full-wave EM simulator, as shown in Fig. 5(a). The antenna was optimized for the desired frequencies inside the capsule- and flat-type devices in the presence of the batteries, sensors, rectifier, and PCB with SMDs. The electrical properties of the skin model were set to be frequency-dependent. The boundaries of the far-field radiation box (overall dimensions of $400 \times 400 \times 400$ mm^3) were kept at least $\lambda_\circ/4$ (where $\lambda_\circ$ is the free-space wavelength calculated at the lower resonant band at 915 MHz) from the edges of

the antenna. Subsequent to the successful optimization of the antenna parameters for the desired frequencies, the proposed self-diplexing antenna (in the capsule- and flat-type devices) was simulated inside a realistic human model. The flat-type device was embedded in a realistic human head (skin implantation), and the capsule-type device was simulated in the intestine (deep tissue implantation). The simulation of the flat-type device was performed considering the practical application of the intracranial pressure measurement, in which the IMD is kept beneath the scalp. The simulation of the capsule-type device was also performed in the human intestine based on the capsule endoscopy, in which a capsule-encased microcamera capture and transmits images from the digestive system (esophagus, stomach, and intestine).

The simulated results (obtained in a homogeneous skin model and heterogeneous realistic human head and intestine) were further validated based on practical measurements. The proposed self-diplexing implantable antenna was designed on an ultrathin (0.13 mm) substrate of Rogers RO3010 with $\epsilon_r = 10.2$ and $\tan \delta = 0.0022$. The antenna was fabricated using a chemical etching process, and the IMDs (capsule- and flat-type devices) were printed using 3-D printing technology. The PCBs inside the IMDs were printed on a commercially available FR-4 laminate ($\epsilon_r = 4.4$), and different types of SMDs were soldered using a standard soldering process. The IMD components (such as the antenna, rectifier, sensors, batteries, and PCB) were packed carefully inside it, and the lid/cap was closed with epoxy glue. The antenna performance was measured in terms of the reflection and transmission coefficients in minced pork and a saline solution, as illustrated in Fig. 5(b). The fabricated antenna was connected with a well-calibrated vector network analyzer (VNA) to measure S_{11}, S_{22}, and S_{21}. The radiation patterns were measured in an anechoic chamber. The measuring system consisted of a signal generator to power a high-gain horn antenna (acting as a Tx antenna), the proposed antenna (operated as a receiving antenna), and a spectrum analyzer. A distance of 1 m was maintained between the Tx and Rx antennas. While measuring the radiation patterns, one port of the antenna was connected to the spectrum analyzer, while the other port was terminated with a 50-Ω load.

4) Simulated and Measured Results of Self-Diplexing Implantable Antenna: Initially, the proposed self-diplexing implantable antenna was simulated and optimized in the homogeneous skin model to reduce the computational time. The sensitivity of the antenna was performed by simulating it in a human head and inside the intestine of a realistic human phantom. The simulated S_{11}, S_{22}, and S_{21} were validated by measuring the fabricated prototype in saline solution and minced pork, as shown in Fig. 5(b). The simulated results in the homogeneous skin model and realistic human model along with the measured results in minced pork and saline solution are shown in Fig. 6(a). Thus, the proposed antenna (simulated and measured results) covered the desired frequency band of industrial, scientific, and medical (ISM) frequency band (915 MHz), when port 1 was excited, and the midfield band (1470 MHz), when port 2 was excited. The lower frequency band had a 10-dB bandwidth of 90 MHz, and the higher
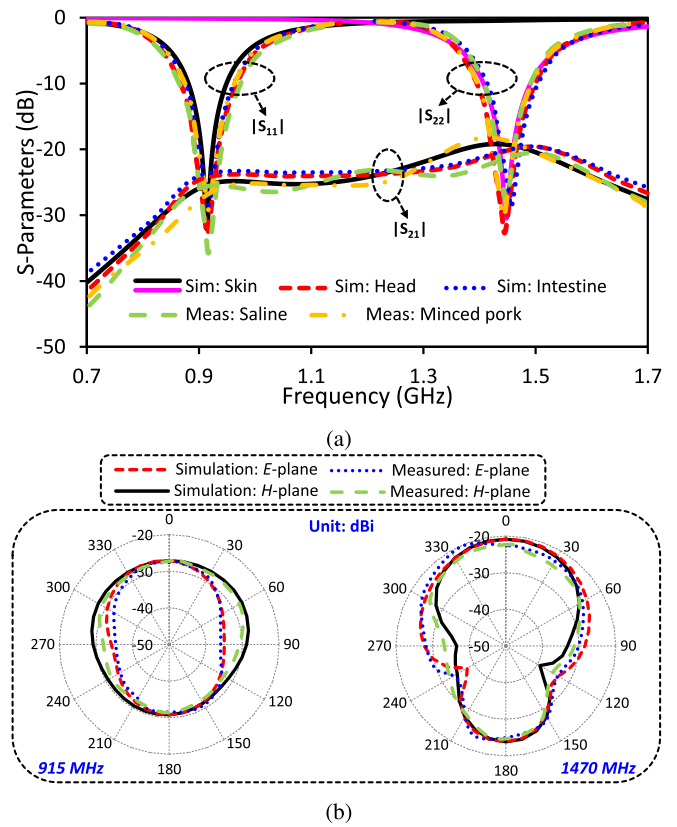

Fig. 6. Simulated and measured antenna results. (a) Reflection coefficients and mutual coupling and (b) radiation pattern in *E*- and *H*-planes at 915 and 1470 MHz.

resonant band had a 10-dB bandwidth of 108 MHz. Isolation of more than 21 dB was observed between both ports. The simulated and measured results showed good agreement. Hence, the lower frequency band (915 MHz) could be used for data communication with an on-body or distant Rx (acting as a transmitting antenna). Port 2 of the self-diplexing antenna was connected with an efficient rectifier for harvesting the EM-radiated power from the WPT Tx at 1470 MHz (acting as a receiving antenna). The receiving and transmitting channels had isolation of more than 21 dB despite the compact design, with an edge-to-edge distance of $0.0038\lambda_{g1}$ (where λ_{g1} is the guided wavelength in the lower frequency band).

In order to evaluate the radiation performance of the proposed self-diplexing antenna, the simulated and measured radiation patterns (*E*- and *H*-planes) are compared at 915 and 1470 MHz, respectively [see Fig. 6(b)]. The figure reflects a good agreement between the simulated and measured results. The simulated (measured) gains of -24.62 dBi (-25.2 dBi) were noted at 915 MHz when port 1 was excited, and those of -18.3 dBi (-19.8 dBi) were noted at 1470 MHz when port 2 was excited. From Fig. 7, it is evident that the radiation patterns of the self-diplexing antenna at both 915 and 1470 MHz frequencies are omnidirectional-like. Due to such radiation patterns, the proposed antenna can receive and transmit data to any arbitrary base station around the patient and receive power from all directions, without affecting (or minimally affecting) the PTE due to misalignment.
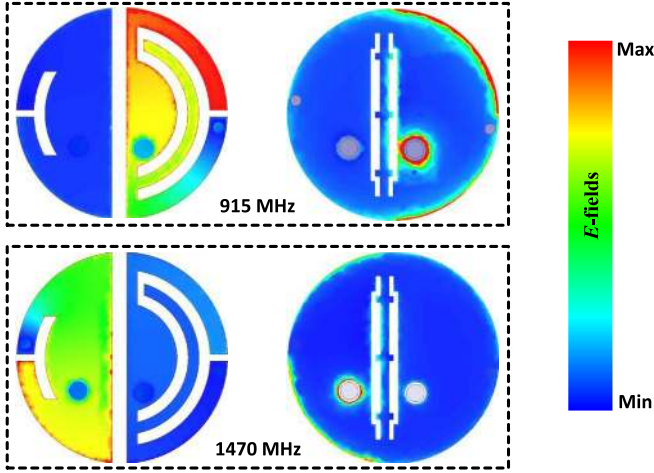
Fig. 7. *E*-fields distribution at 915 (when port 1 is excited) and 1470 MHz (when port 2 is excited).

Fig. 8. Comparison of theoretical and measured link received powers.

TABLE II

PARAMETERS FOR BIOTELEMETRIC RECEIVED POWER

Variables	Description (Units)	Values
f	Frequency (MHz)	915
P_t	Transmitted power (dBm)	-16
G_t	Implantable antenna gain (dBi)	-24.62
G_r	Receiver antenna gain (dBi)	2
γ	Path loss exponent	1.5
X_σ	Shadowing factor	4
d	Distance (m)	0-2
L_{feed}	Feed losses (dB)	2
L_{pol}	Polarization loss (dB)	0.3

The *E*-field distributions of the antenna are shown in Fig. 7, which depicts the *E*-field distributions at 915 MHz when port 1 was excited and at 1470 MHz when port 2 was excited. At 915 MHz, the *E*-fields are quasi-evenly distributed on the excited patch with maximum fields on the X+ and Y+ coordinates, and the *E*-field distributions on the ground plane below the excited patch are more than that on the other side. At 915 MHz, the *E*-fields are quasi-evenly distributed on the excited patch with maximum fields on the X− and Y− coordinates. The distribution of the field on the ground follows the same pattern but on the opposite side, as for 915 MHz. It is observed that nearly zero fields are coupled to the other radiator when one radiator is excited, which further confirms the high isolation between the radiators.

5) Evaluation of the Telemetric Performance of the Self-Diplexing Antenna: Reliable communication is an essential factor in implantable biotelemetry. The implanted antenna must transmit real-time recorded data. To confirm the performance of the wireless telemetry of the proposed antenna, we studied the transmission ability of the proposed antenna theoretically and practically. The fundamental parameters for studying the co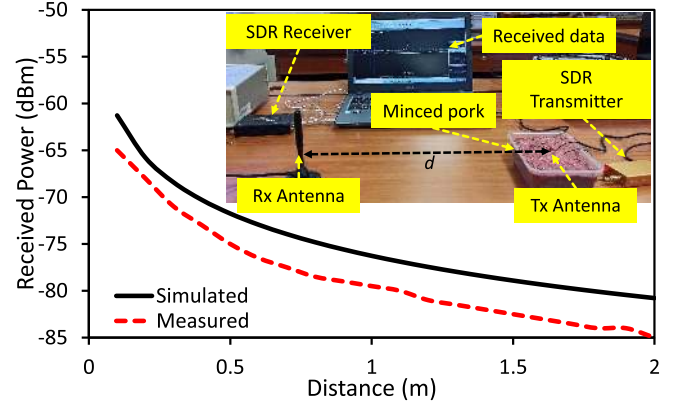mmunication link are listed in Table I. In this scenario, the self-diplexing implantable antenna acted as a transmitting antenna, and a monopole antenna acted as a receiving antenna. The distance between the receiving and transmitting antennas was varied to record the received power. We used (4) to calculate the received power [33] as follows:

$$P_r(\text{dBm}) = P_t + G_t + G_r - L_{\text{feed}} - L_{\text{pol}} - \text{PL} \tag{3}$$

$$\text{PL(dB)} = 10\gamma \log_{10}\left(\frac{d}{d_\circ}\right) + 20\log_{10}\left(\frac{4\pi d_\circ}{\lambda_\circ}\right) + X_\sigma . \tag{4}$$

The elements of (4) are listed in Table II.

The practical implementation was performed by connecting the implantable antenna with a transmitting software-defined radio (SDR), and a monopole antenna with a gain value of 2 dBi was connected to a receiving SDR, as shown in Fig. 8. A narrow bandwidth signal of 20 MHz was generated through a transmitting SDR and propagated through the implantable antenna. The distance (*d*) between both antennas was varied, and the received power was recorded. The implantable antenna successfully communicated with the external Rx. The theoretical and practical values of the received power were compared, as shown in Fig. 8. The practical values agree with the theoretical ones. The difference between both values is due to environmental effects.

B. Wireless Power Transfer Transmitter

The purpose of the WPT Tx is to track and direct the maximum power to the deep-tissue IMD. For this purpose, a specific WPT Tx needs to be designed, i.e., one that can direct its radiated power on mm-sized implants [23]. We designed our WPT Tx with a patterned patch and full ground plane. The front, back, and side views of the proposed WPT Tx are shown in Fig. 9. The WPT Tx was designed on a commercially available FR-4 substrate ($\epsilon_r = 4$ and thickness = 1.6 mm) with overall dimensions of $50 \times 50 \times 1.6$ mm^3. We assigned two ports on diagonals with a 180° phase difference, as the appropriate phase in multiport operation leads to direct radiation of power on the desired place. We assigned only two ports with a 180° difference, as we were considering static IMDs. In the case of moving IMDs, such as leadless pacemakers and capsule endoscopy, a quad-port
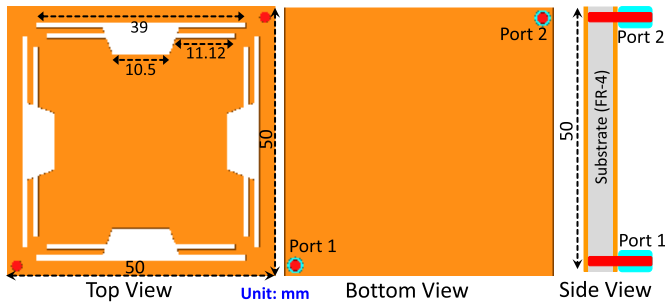
Fig. 9. Schematic (top, bottom, and side views) of the proposed WPT transmitter.

operation with diverse phase combinations is required to track and direct the radiated power to the IMD.

The simulation setup of the WPT Tx is different from that of free-space antennas, as shown in Fig. 10(a). We kept the WPT Tx at a distance of 5 mm from the homogeneous skin model and faced the WPT Tx patch toward the deep-tissue IMD. The IMD was placed deep inside (55-mm deep) the homogeneous skin model. The mismatch between the permittivity of the air (low permittivity) and that of the skin (high permittivity) caused power leakage. Different approaches have been suggested to minimize such power leakages. Such approaches include flexible and conformal surfaces [12], passive patches [28], negative-μ metamaterial [34], [35], and a high-dielectric-constant matching layer [25]. A high-dielectric-constant matching layer is used to minimize the power leakage and enhance the PTE. A matching layer with high permittivity was designed on the outer side of the homogeneous skin model to improve the received power. The total gap between the IMD and WPT Tx was 60 mm. The WPT Tx was optimized at 1470 MHz in this setup. The simulation and measured results showed a wideband response (1250–1680 MHz), as shown in Fig. 10(c). The optimized WPT Tx was fabricated on an FR-4 substrate using a chemical etching process, and "subminiature version A" (SMA) connectors were soldered at designated places.

The measured results of the WPT Tx were obtained by placing the IMD deep inside the minced pork; WPT Tx was also placed outside the container filled with minced pork. The WPT Tx was connected with a power divider to provide equal amplitude signals to both ports but with a phase difference of 180°. The measurement setup and fabricated WPT Tx prototype are shown in Fig. 10(c). Fig. 10(b) shows the surface current distribution of the WPT Tx at 1470 MHz when two ports were excited with equal magnitude and a 180° phase difference. Our proposed WPT Tx has all the desired characteristics for coupling the current density with the human tissue (as suggested in [36]). The phase difference between the ports can be used to control the beamwidth and directivity, as shown in Fig. 11. The phase difference can be adjusted to direct the beam from WPT Tx to IMD in order to minimize the misalignment effects. It is worth mentioning here that we are considering a static implant with a minimal misalignment factor. Therefore, a small change in beamwidth and directivity is enough for power transfer. However, in the case of moving
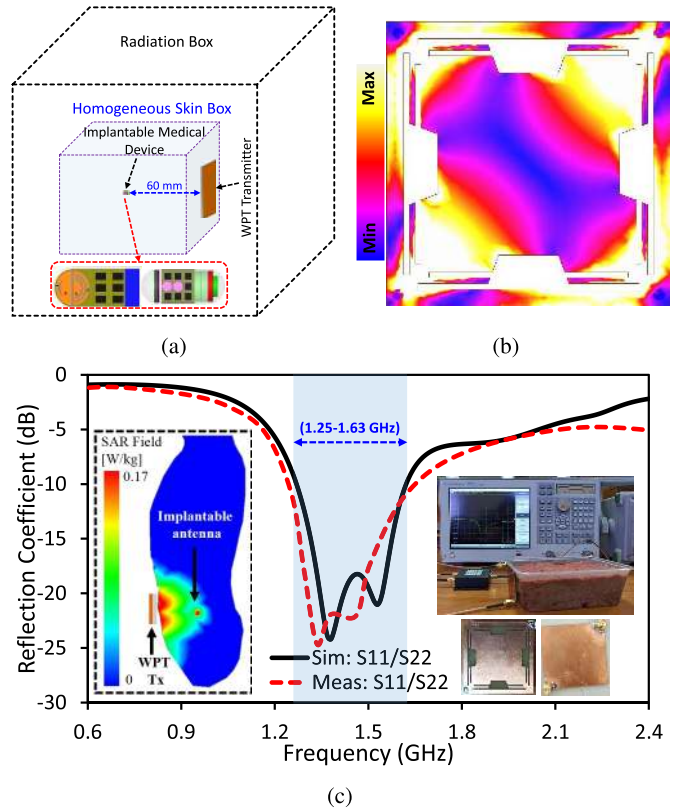

Fig. 10. (a) Simulation setup and (b) surface current distribution of the WPT Tx at 1470 MHz when two ports were excited with equal magnitude and 180° phase difference and (c) simulated and measured reflection coefficient of WPT TX, fabricated prototype, 1-g SAR results, and measurement setup.

IMDs, such as leadless pacemakers and capsule endoscopy, a quad-port operation with diverse phase combinations is required to track and direct the radiated power to the IMD [9].

On the other hand, the specific absorption rate (SAR) analysis is a critical part of ensuring human safety. Therefore, the radiation in the vicinity of the human body is regulated by IEEE and the International Commission on Non-Ionizing Radiation Protection (ICNIRP), so as to not exceed certain SAR limits (1.6 W/kg averaged over 1 g and 2 W/kg averaged over 10 g of tissue, respectively). We evaluated the safety of our system in terms of 1-g SAR at both frequencies (915 and 1470 MHz). Hence, on the implant side, the antenna was transmitting at 915 MHz, whereas, at 1470 MHz, it acted as receive-only for the WPT. Therefore, a 1-g SAR analysis for the implantable self-diplexing antenna was conducted inside torso and head models at 915 MHz, as shown in Fig. 12. However, at 1470 MHz, the 1-g SAR was analyzed for the WPT Tx. This is because, at this band, the implantable antenna is passive, while the WPT Tx is radiating. As shown in Fig. 12, the peak values of the 1-g SAR in the torso and head models at 915 MHz were 331.4 and 295.2 W/kg, respectively. The peak SAR in the head was lower than that in the torso because the antenna implantation depth was much lower than that in the torso; thus, less EM energy was absorbed by the tissue. For the WPT Tx transmission mode at 1470 MHz, the maximum SAR value of 0.17 W/kg, as averaged over 1-g tissue, was noted at 1470 MHz, as shown in Fig. 10(c). All of these SAR values
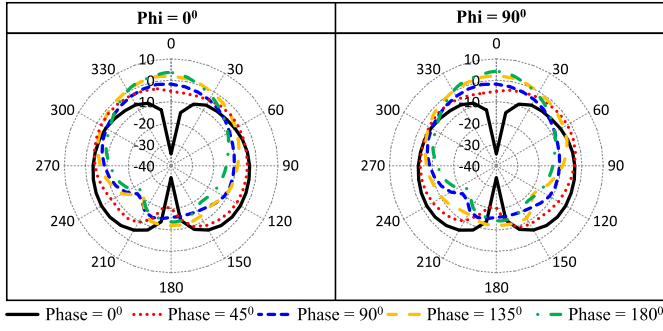
Fig. 11. Radiation pattern of the WPT Tx at 1470 MHz with different phase differences.
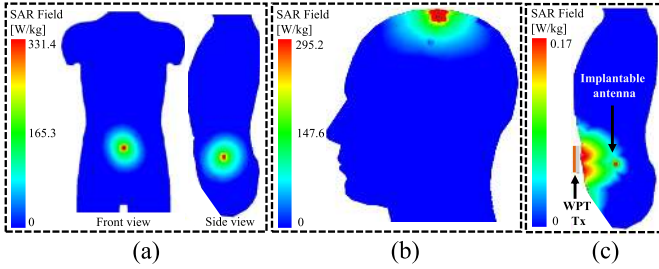

Fig. 12. SAR distributions averaged over 1-g of tissue in human torso and head anatomical models. (a) Coronal and sagittal distributions of 1-g SAR in man torso, (b) Sagittal 1-g SAR distribution on head anatomical model, and (c) SAR distribution of WPT transmitter.

were calculated when 1 W of power was provided to each port. As the maximum allowable radiated power of the medical implants is limited to 25 μW by ICNIRP, the allowable power computed from the peak SAR are higher, which confirms that the antenna is safe even if it radiates up to 4.5 mW in the abdomen and 5.4 mW in the head, respectively. Moreover, the proposed WPT Tx is safe even if the supplied power is 9.4 W (under the 1-g tissue guidelines).

C. Rectifier Circuit Design

A rectifier circuit converts RF energy to suitable dc energy that can be used to charge and drive deep-tissue IMDs. A rectifying circuit consists of a rectifying topology, load, and input and output filters. IMDs require a low-powered and efficient rectifier circuit to drive or charge the electronic components. In this study, the rectifier circuit is designed in the Keysight ADS, as shown in Fig. 13. The main aim of rectifier circuit design was to maximize the power transfer to the rectifier circuit by minimizing the return loss and enhancing the RF-dc conversion efficiency. The rectifier circuit was excited with a 50-Ω input impedance to provide simple and easy integration of the self-diplexing implantable antenna in the later stage. The reflection coefficient was determined using the following:

$$\Gamma = \frac{Z_{in} - Z_o}{Z_{in} + Z_o} \tag{5}$$

where Γ is the reflection coefficient of the rectifier, Z_{in} is the input impedance of the rectifier, and $Z_o = 50\Omega$ is the source impedance [see Fig. 13(b)]. The maximum power will be transferred to the rectifier circuit if the source impedance (50 Ω) is the same as the rectifier impedance.
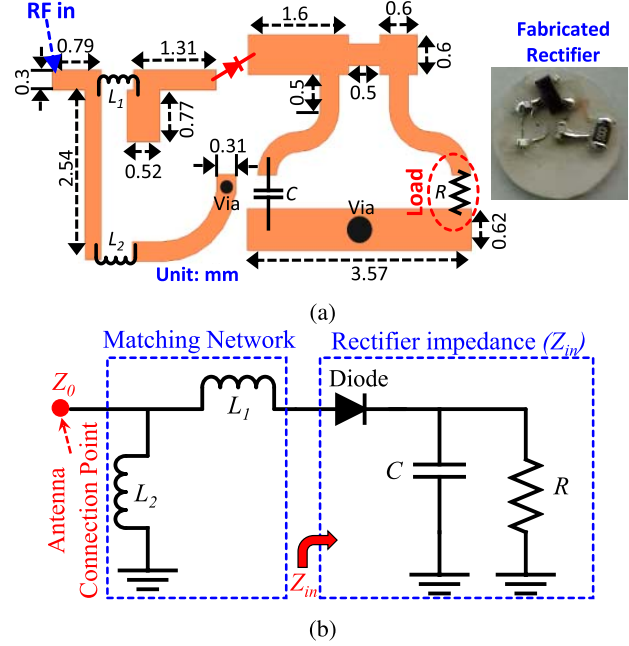

Fig. 13. (a) Complete schematic and fabricated prototype of the rectifier and (b) equivalent circuit of the rectifier (L_1 = 22 nH (parasitic resistance = 2.85Ω, quality factor = 9, and part number = LQP03TG22NH02), L_2 = 4 nH (parasitic resistance = 0.40Ω, quality factor = 10, and part number = MHQ0402PSA4N0BT000), R = 2 kΩ, and C = 12 pF).

The RF-dc conversion efficiency shows the ability of a rectifier to convert RF power to dc power and is given as follows [37]:

$$\eta(\%) = \frac{P_{out}}{P_{in}} \times 100\% = \frac{V^2}{P_{in} \times R_L} \times 100\%. \tag{6}$$

Here, $\eta(\%)$ is the RF-dc conversion efficiency ($\eta_{RF\text{-}dc}$ in percentage), P_{out} is the output dc power of the rectifier, P_{in} is the input power to the rectifier (received power by Rx from the WPT Tx), V is the output dc voltage, and R_L is the resistive load.

A schematic of the proposed rectifier circuit is shown in Fig. 13. The HSMS-2852 diode was selected, as it offers a fast switching operation. The matching between the input source and rectifier was optimized through a series inductor (L_1) and short-circuited stub. An inductor (L_2) is shunted at the circuit's input for the dc return path. A shunt-mounted capacitor (C) is used as an output filter, and a resistor (R) is used as a load. The HSMS-2852 diode is suitable for low-powered applications, as it has a low junction capacitance (C) and minimum sensitive voltage [38], [39]. The operating frequency (f_o) and input voltage (V_{in}) regulate the value of C.

The proposed rectifier was designed using a unique second-order L-section matching network comprising two inductor elements: L_1 and L_2. For a proper matching network, the equivalent transmission line from the source L_2 is given as [40] follows:

$$R_{ant} = R_{in} \cdot \left(\frac{1}{1 + Q^2} \right). \tag{7}$$

Here, R_{in} = rectifier input resistance, R_{ant} = source resistance (antenna resistance), and the quality factor Q is determined as follows:

$$Q = \sqrt{\frac{R_{in}}{R_{ant}} - 1}. \qquad (8)$$

To determine the value of L_2, we use the main relationship for the quality factor as the ratio of the imaginary part to the real part, as follows:

$$Q = \frac{I_m(Z)}{R_e(Z)} = \frac{I_m\left(\frac{1}{\frac{1}{j\omega_o L_2} + j\omega_o X_{in} + \frac{1}{R_{in}}}\right)}{R_e\left(\frac{1}{\frac{1}{j\omega_o L_2} + j\omega_o X_{in} + \frac{1}{R_{in}}}\right)}$$
$$= \omega_o R_{in}(L_2 + X_{in}). \qquad (9)$$

In the above, X_{in} = reactive component of the rectifying circuit operating at an angular frequency ω_o. The inductance L_2 of the network is determined as follows:

$$L_2 = \left(\frac{Q}{\omega_o R_{in}}\right) - X_{in}. \qquad (10)$$

The L-section inductor L_1 is computed from the parallel to the series transformation and by equating the equivalent imaginary part to zero, as follows:

$$j\omega_o L_1\left(\frac{Q^2}{1+Q^2}\right) + j\omega_o L_2 + \frac{1}{j\omega_o X_{in}(1+Q^2)} = 0. \qquad (11)$$

L_1 can be express from (11) as

$$L_1 = \frac{1}{\omega_o^2 X_{in}} - L_2\left(\frac{R_{in}}{R_{in} - R_{ant}}\right). \qquad (12)$$

The optimization of the proposed schematic was performed in Keysight ADS, in consideration of the two goals for maximum power transfer to the rectifier circuit, i.e., minimizing the return loss and enhancing the RF-dc conversion efficiency. Each parameter, including the microstrip traces and lumped element values, was tuned to achieve the desired results. The optimized parameters are provided in Fig. 13. A thin (0.625 mm) and high dielectric constant ($\epsilon_r = 10.2$) material comprised of Rogers RO 3010 ($\tan \delta = 0.0022$) was used as a substrate in the rectifier.

The optimal load resistance of the rectifier was analyzed by sweeping load resistance (R). Fig. 14 shows the RF-dc conversion efficiency as a function of load resistance (R) for different input powers. It can be noted from the figure that RF-dc conversion efficiency is dependent on the load resistance (R). The efficiency of the rectifier increased until 2 KΩ and then dropped down for higher values. It can be observed that the efficiency of the rectifier is always higher at 2 KΩ for different input power values; thus, this is the optimal load resistance for the rectifier. Furthermore, it is worth mentioning here that the RF-dc conversion efficiency of the rectifier was 72 % at the load resistance of 13 KΩ when the input power was 2 dBm. Therefore, the proposed rectifier is a suitable choice for a power management unit (PMU) whose resistance is high (typically around 10 kΩ).

Fig. 15 shows the return loss and impedance of the rectifier as a function of frequency. It operates at 1470 MHz with a
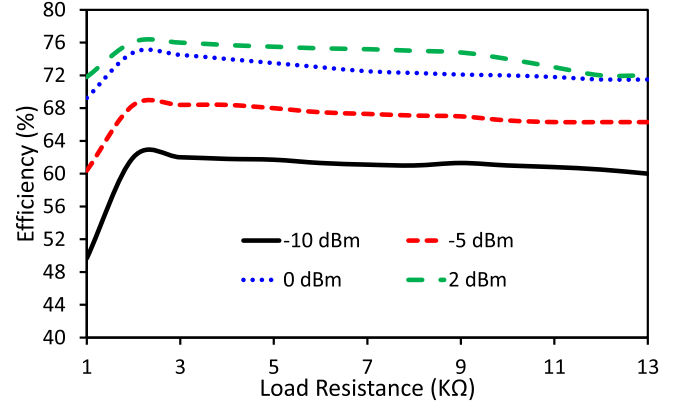
Fig. 14. Maximum RF-dc conversion efficiency at corresponding input power at different load resistances.
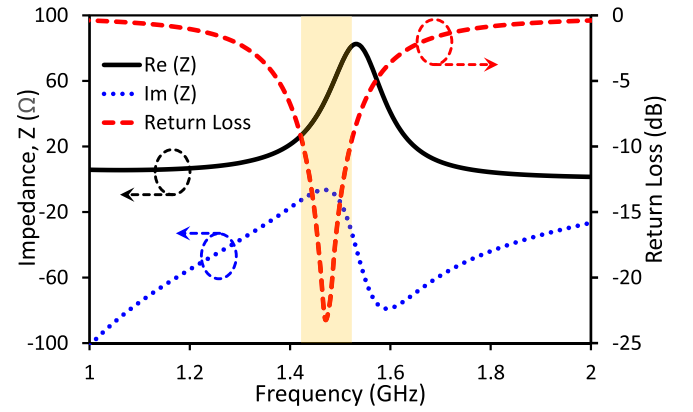
Fig. 15. Impedance (real and imaginary parts) and return loss of the rectifier as a function of frequency.
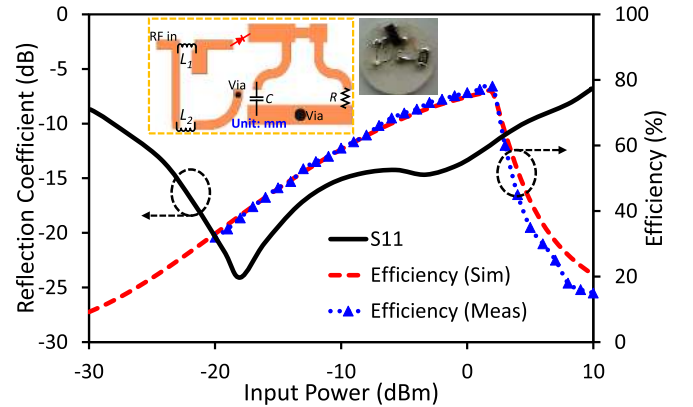
Fig. 16. Simulated reflection coefficient as a function of input power, and simulated and measured RF-dc efficiency.

10-dB bandwidth of 108 MHz (1420–1528 MHz). Fig. 16 plots the reflection coefficient against the varying input power. As shown, the proposed rectifier has sufficient impedance matching over a wide range of input power. The reflection curve is lower than −10 dB for the input power ranging from −28 to 5 dBm. The RF-dc conversion efficiency (as a function of the input power) is shown in Fig. 16. We used (6) to

Fig. 17. DC output voltage across the load (2 kΩ and 10.9 kΩ) as a function of input power.

Fig. 18. Simulated (solid line) and measured (dashed line) s-parameters of WPT Tx (S_{11}) and self-diplexing implantable antenna (S_{22}).

determine the measured RF-dc conversion efficiency. While measuring the performance of the rectifier circuit, the input port of the rectifier was connected to a signal generator, and the output was connected to a digital multimeter (DMM). We placed the rectifier inside the IMD below the antenna, and the IMD was kept deep inside the minced pork, as shown in Fig. 17. Different values of input power were generated through the signal generator, and the output was analyzed through DMM. It can be seen that the RF-dc conversion efficiency is better than 50% for a wide range of input power (from −14 to 5 dBm). Hence, the proposed rectifier circuit exhibited high conversion efficiency (50% efficiency even at a low input power of −14 dBm and peak efficiency of 76.1% at 2 dBm). The capability to sense low input power and the high RF-dc conversion efficiency (>50% efficiency from −14 to 5 dBm) makes this rectifier a suitable candidate for low-powered communication devices, such as IMDs. The dc output voltage across the load (2 kΩ and 10.9 kΩ), as a function of the input power, is shown in Fig. 17. The simulated results agree well with the measured ones. Furthermore, reverse diode current was found to be −3.5 mA at an input power of 3 dBm (saturation voltage of 1.47 V).
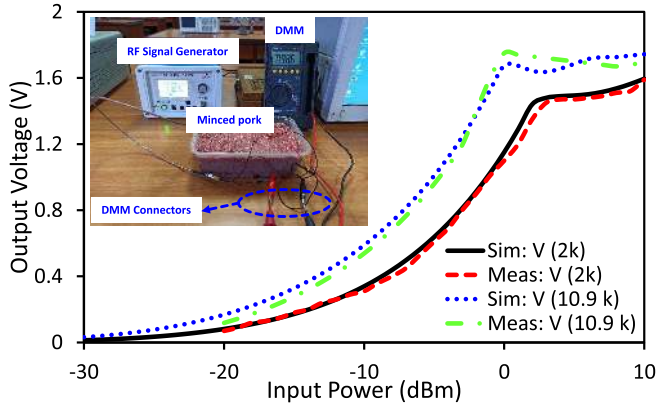
III. RESULTS AND DISCUSSION

Initially, each component of the WPT system (self-diplexing implantable antenna, a rectifier circuit, and WPT Tx) was separately optimized and experimentally validated. The self-diplexing implantable antenna was designed for 915 and 1470 MHz. The antenna was integrated into IMDs (capsule-type and flat-type). The antenna performance was analyzed in a homogeneous skin model and in a realistic human head and intestine. The S-parameters of the antenna were measured in the minced pork and saline solution, whereas the radiation pattern was measured only in the minced pork because to easily handle the setup inside the anechoic chamber.

A WPT Tx was designed in the next step. We kept the WPT Tx at a distance of 5 mm from the homogeneous skin model and faced the WPT Tx patch toward the deep-tissue IMD. The total gap between the IMD and WPT Tx was 60 mm. In this step, the antenna inside the IMD was not excited;
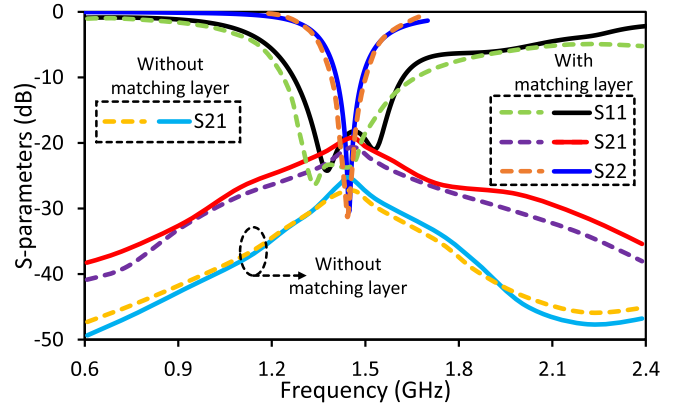
only the WPT Tx was excited (simulation). The measured results from the WPT Tx were obtained by placing the WPT Tx outside of the container containing the minced pork. The WPT Tx was connected with a power divider to provide equal amplitude signals to both ports but with a phase difference of 180°. Then, a cosimulation of the self-diplexing implantable antenna and WPT Tx was performed. We kept the WPT Tx at a distance of 5 mm from the homogeneous skin model and faced the WPT Tx patch toward the deep-tissue IMD. The IMD was placed deep inside (55-mm deep) the homogeneous skin model. A matching layer with a high permittivity was designed on the outer side of the homogeneous skin model to improve the received power. The simulated and measured results of WPT Tx and self-diplexing antenna are given in Fig. 18. Initially, the WPT system (WPTS) was evaluated without the matching layer (Rogers 3010, dielectric constant = 10.2); S_{11} and S_{22} were well-matched. In this case, S_{21} of the system was −26.2 dB at 1470 MHz. A major part of the power was reflected back to the WPT Tx due to the dielectric mismatch, which significantly reduces the PTE (PTE is dependent on the value of S_{21}). Finally, in order to maintain minimum dielectric mismatch, a matching layer was introduced over the human body. The S_{21} value was increased from −26.2 to −19.7 dB (increase of 6.5 dB); thus, the PTE was enhanced from 0.2% to 1.07%. Moreover, the matching layer has no significant effect on S_{11} and S_{22} of the WPTS. However, it slightly increases the SAR and temperature of the human body. The matching layer increases the E-field penetration, which causes an increase in the SAR and temperature value. The SAR value increased from 0.11 to 0.17 W/Kg, and the temperature rise increased from 0.423 to 0.61 °C. The slight increase in SAR and body temperature is negligible as both values lie within the specified limits (SAR ≤ 1.6 W/Kg and temperature rise ≤ 2 °C). Table IV lists the performance comparison with and without the matching layer. As shown, the simulation and measured results are matched. While measuring, the WPT Tx was placed on the side of the container containing the minced pork, and the IMD was placed deep inside the minced pork. The WPT Tx was connected with power divider to provide equal amplitude signals to both ports but with a phase difference of 180°,

TABLE III
COMPARISON OF THE PROPOSED WPT SYSTEM WITH THE PUBLISHED LITERATURE

	Comparison Parameters	[8]	[9]	[11]	[12]	[19]	[25]	[26]	[28]	Proposed Work
WPT System	Operating Frequency	2.4 GHz	1.5 GHz	1.5 GHz	1.5 GHz	400 MHz	1470 MHz	1900 MHz	2.45 GHz	**1470 MHz**
	WPT Technique	Midfield	Midfield	Midfield	Midfield	Near-field	Midfield	Near-field	Far-field	**Midfield**
	Transfer Distance	2.5 mm	55 mm	55 mm	4 cm	3 mm	50 mm	20 cm	50 mm	**60 mm**
	Tx Power	4 mW	1 W	1 W	800 mW	19 mW	1 W	1 W	1 W	**1 W**
	Received Power (mW)	0.6	2.9	5.6	0.83	--	6.7	2.5	--	**10.7**
	$|S_{21}|$	--	-23.5 dB	-22.5	--	-30.81 dB	-21.7 dB	-25.9 dB	-41.3 dB	**-19.7 dB**
	PTE (%)	15	0.473	0.56	0.1	0.084	0.67	0.25	0.007	**1.07**
	SAR (W/Kg)	0.368 (1-g)	--	1.29 (10-g)	--	1.5 (1-g)	0.187 (1-g)	--	0.145 (1-g)	**0.17 (1-g)**
Rectifier	Type	--	--	--	Voltage doubler	--	Voltage doubler	Voltage doubler	One diode topology	**One diode topology**
	Conversion Efficiency	--	--	--	--	--	90% at 2 dBm	82% at 2 dBm	42% at -10 dBm	**76.1% at 2 dBm**
WPT Tx	Type	Patch	Patch	Slotted patch	Phased surface	Coil	Slotted patch	Spiral coil	Patch	**Slotted patch**
	Size (cm²)	1.01 x 1.88	6.3 x 6.3	6.5 x 6.5	6.3 x 6.3	--	6 x 6	5 x 5	--	**5 x 5**
Implantable Antenna	Operation bands	Single band	Quad band	Single band	Single band	Single band	Quad band	Dual band	Single band	**Dual band**
	Volume (mm³)	1632	31.77	93.6	12	--	8.43	6.72	12.90	**9.4**
	Gain (dBi)	--	-34.6	-26	--	--	-34, -19.6,-28.2, and -22.4	-26.8, and -18.8	-19	**-24.62, and -18.3**
	Bandwidth (%)	--	--	--	--	0.7	--	9.83, and 27.9	4.1	**9.8, and 7.34**
	SAR1g (W/Kg)	--	410	--	--	--	--	344.25, and 629.8	--	**331.4, and 241.1**
	Antenna Type	Patch	Patch	Patch	Coil	Coil	Slotted patch	Spiral patch	Patch	**Slotted patch**
	Ground plane	--	Full	Slotted	--	--	Slotted	Slotted	Full	**Slotted**
	Simultaneous Telemetry & Powering	No	No	No	No	No	No	No	No	**Yes**
	External Multiplexer for Operation	Yes	Yes	Yes	Yes	Yes	Yes	No	Yes	**No**

TABLE IV
COMPARISON OF THE WPTS PARAMETERS WITH AND
WITHOUT THE MATCHING LAYER AT 1470 MHz

Parameter	Without Matching layer	With matching layer
Input Power (W)	1	1
S_{21} (dB)	-26.2	-19.7
PTE (%)	0.2	1.07
Received Power (mW)	2	10.7
SAR-1g (W/Kg)	0.11	0.17
Temprature Rise (°C)	0.423	0.61

and one port of the self-diplexing implantable antenna was connected to a network analyzer. The PTE of the WPT system was evaluated through S-parameters using (13)–(14) [41]. Equation (14) is widely used to determine the maximum PTE of the WPT systems. As shown in Fig. 18, the proposed WPT Tx has S_{11} less than −18 dB at the targetted frequency of 1470 MHz. The S_{11} curve shows the reflected power from

the WPT Tx toward the port, and S_{11} being less than −18 dB assures that more than 99% of the power was radiated by the WPT Tx. The S_{11} term in (13) was ignored because of sufficient impedance matching, and thus, we calculated our PTE using (14) [25]. The simulated (measured) S_{21} value of the WPT system was −19.7 dB (−20.4 dBi) at 1470 MHz, as shown in Fig. 18. The simulated (measured) maximum PTE of the WPT system was recorded as 1.07% (0.91%) at 1470 MHz

$$\text{PTE} = \frac{|S_{21}|^2}{1 - |S_{11}|^2} \qquad (13)$$

$$\text{PTE} = |S_{21}|^2 \qquad (14)$$

where $|S_{11}|$ is the reflection coefficient of the WPT Tx, and $|S_{21}|$ is the transmission coefficient between WPT Tx and self-diplexing implantable antenna. Moreover, the efficiency of overall WPTS can be evaluated by multiplying the WPT efficiency (PTE) with the rectifier efficiency ($\eta_{\text{RF-dc}}$) using (15) [42]. The overall efficiency of the WPTS is 0.81% for the input power of 0 dBm

$$\eta_{\text{sys}} = |S_{21}|^2 \times \eta_{\text{RF-dc}} . \qquad (15)$$

To demonstrate the wireless powering capability of the WPT Tx system, Port 2 of the self-diplexing implantable antenna was connected to the proposed rectifier using a 50-Ω SMA connector. The output voltages at 1470 MHz at different power levels were measured. The implantable antenna, integrated with the rectifier circuit along with the necessary components of IMD, was enclosed in a casing of the IMD. The IMD was placed deep inside the container containing the minced pork. The matching layer was placed on the side of the same container. The WPT Tx was placed on the side of the container containing the IMD deep inside the minced pork. The WPT Tx was connected to a power divider to provide equal amplitude signals to both ports but with a phase difference of 180°. One port of the WPT Tx was connected with a signal generator to transfer different levels of power to WPT Tx at 1470 MHz. A DMM was connected at the output of the rectifier to record the output voltage.

A dc–dc boost converter (BC) and power management unit (PMU) are required in real applications to regulate and transfer dc power to electronic and storage devices, such as batteries and sensors. It is known that the voltage obtained from the rectenna is unstable. Therefore, we need a compact BC and PMU before supplying dc power to the components in the IMD. We selected the PMU module BQ25570 (Texas Instruments): this PMU module has an input impedance of 10.9 kΩ and requires a starting current of approximately 330 nA, the voltage of 330 mV, and the input power of 10 μW. In view of the input impedance of the PMU module, we changed the load impedance to 10.9 kΩ; the other rectifier components remained unchanged. The output voltage of the rectifier as a function of the input impedance at the load of 10.9 kΩ is shown in Fig. 17. At −10 dBm, the dc voltage is equal to 588 mV, and the current is equal to 53.96 μA. Our proposed rectifier integrated self-diplexing antenna fulfills the PMU requirement, and thus, the boost converted may be self-started.

A comprehensive comparison between the proposed WPT system and existing WPT systems is presented in Table III. It is obvious that the proposed system has clear advantages over existing systems due to its ability to simultaneously manage biotelemetry and wireless powering. The conventional implantable antennas can either transmit or receive data in all bands at the same instance, and an external multiplexer is required for independent transmission and reception in all bands. IMDs have minimal space, and an additional multiplexer increases the complexity and size. Our proposed self-diplexing antenna can simultaneously operate in dual modes (transmission and reception). In addition, there is no external circuitry (multiplexer circuit) required in our proposed self-diplexing antenna, and thus, the compactness is maintained.

IV. CONCLUSION

In this article, a novel WPT system was proposed by introducing a self-diplexing antenna system to medical implants. A compact semicircular self-diplexing antenna was designed at 915 and 1470 MHz. The patch operating at 1470 MHz was connected to the rectifier circuit for harvesting EM waves from the WPT Tx at 1470 MHz. Compared to the reported antennas in the literature, the self-diplexing implantable antenna can transfer data and harvest the power radiated by on-body WPT Tx simultaneously without using extra multiplexing, circulator, and filter circuits. The IMD, consisting of a self-diplexing antenna and rectifier, was evaluated in a realistic human head and intestine. Moreover, the simulated results were verified by measuring the IMD in the minced pork and saline solution. The WPT Tx was optimized at 1470 MHz. Each component of the WPT system was individually measured to verify the simulated results. As a system, the WPT system was measured by placing an IMD deep in the container containing minced pork, and the WPT Tx was placed on the side of a container containing the IMD deep inside the minced pork. Considering the real applications, analyses were carried out and successfully verified by considering the BQ25570 module as the PMU. It is concluded that the proposed system simplifies the implantable device and is capable of simultaneously transferring data from impaired organs and powering the electronic components in IMDs.

REFERENCES

[1] K. Agarwal, R. Jegadeesan, Y.-X. Guo, and N. V. Thakor, "Wireless power transfer strategies for implantable bioelectronics," *IEEE Rev. Biomed. Eng.*, vol. 10, pp. 136–161, 2017.

[2] S. A. A. Shah and H. Yoo, "Scalp-implantable antenna systems for intracranial pressure monitoring," *IEEE Trans. Antennas Propag.*, vol. 66, no. 4, pp. 2170–2173, Apr. 2018.

[3] A. Basir, M. Zada, and H. Yoo, "Compact and flexible wideband antenna for intraoral tongue-drive system for people with disabilities," *IEEE Trans. Antennas Propag.*, vol. 68, no. 3, pp. 2405–2409, Mar. 2020.

[4] A. Basir and H. Yoo, "A stable impedance-matched ultrawideband antenna system mitigating detuning effects for multiple biotelemetric applications," *IEEE Trans. Antennas Propag.*, vol. 67, no. 5, pp. 3416–3421, May 2019.

[5] R. Das and H. Yoo, "Biotelemetry and wireless powering for leadless pacemaker systems," *IEEE Microw. Wireless Compon. Lett.*, vol. 25, no. 4, pp. 262–264, Apr. 2015.

[6] X. Y. Liu, Z. T. Wu, Y. Fan, and E. M. Tentzeris, "A miniaturized CSRR loaded wide-beamwidth circularly polarized implantable antenna for subcutaneous real-time glucose monitoring," *IEEE Antennas Wireless Propag. Lett.*, vol. 16, pp. 577–580, 2017.

[7] B. Biswas, A. Karmakar, and V. Chandra, "Miniaturised wideband ingestible antenna for wireless capsule endoscopy," *IET Microw., Antennas Propag.*, vol. 14, no. 4, pp. 293–301, Mar. 2020.

[8] W.-C. Chen, C. W. L. Lee, A. Kiourti, and J. L. Volakis, "A multi-channel passive brain implant for wireless neuropotential monitoring," *IEEE J. Electromagn., RF Microw. Med. Biol.*, vol. 2, no. 4, pp. 262–269, Dec. 2018.

[9] R. Das and H. Yoo, "A multiband antenna associating wireless monitoring and nonleaky wireless power transfer system for biomedical implants," *IEEE Trans. Microw. Theory Techn.*, vol. 65, no. 7, pp. 2485–2495, Jul. 2017.

[10] K. Bazaka and M. Jacob, "Implantable devices: Issues and challenges," *Electronics*, vol. 2, no. 4, pp. 1–34, Dec. 2012.

[11] N. Nguyen, N. Ha-Van, and C. Seo, "Midfield wireless power transfer for deep-tissue biomedical implants," *IEEE Antennas Wireless Propag. Lett.*, vol. 19, no. 12, pp. 2270–2274, Dec. 2020.

[12] D. R. Agrawal *et al.*, "Conformal phased surfaces for wireless powering of bioelectronic microdevices," *Nature Biomed. Eng.*, vol. 1, no. 3, p. 0043, Mar. 2017.

[13] C.-S. Wang, G. A. Covic, and O. H. Stielau, "Power transfer capability and bifurcation phenomena of loosely coupled inductive power transfer systems," *IEEE Trans. Ind. Electron.*, vol. 51, no. 1, pp. 148–157, Feb. 2004.

[14] P. Li and R. Bashirullah, "A wireless power interface for rechargeable battery operated medical implants," *IEEE Trans. Circuits Syst. II, Exp. Briefs*, vol. 54, no. 10, pp. 912–916, Oct. 2007.

[15] C.-S. Wang, O. H. Stielau, and G. A. Covic, "Design considerations for a contactless electric vehicle battery charger," *IEEE Trans. Ind. Electron.*, vol. 52, no. 5, pp. 1308–1314, Oct. 2005.

[16] A. Munir and B. T. Ranum, "Wireless power charging system for mobile device based on magnetic resonance coupling," in *Proc. Int. Conf. Electr. Eng. Informat. (ICEEI)*, Aug. 2015, pp. 221–224.

[17] J. Garnica, R. A. Chinga, and J. Lin, "Wireless power transmission: From far field to near field," *Proc. IEEE*, vol. 101, no. 6, pp. 1321–1331, Jun. 2013.

[18] R. Jegadeesan and Y.-X. Guo, "Topology selection and efficiency improvement of inductive power links," *IEEE Trans. Antennas Propag.*, vol. 60, no. 10, pp. 4846–4854, Oct. 2012.

[19] M. Manoufali, K. Bialkowski, B. J. Mohammed, P. C. Mills, and A. Abbosh, "Near-field inductive-coupling link to power a three-dimensional millimeter-size antenna for brain implantable medical devices," *IEEE Trans. Biomed. Eng.*, vol. 65, no. 1, pp. 4–14, Jan. 2018.

[20] R. Jegadeesan, K. Agarwal, Y.-X. Guo, S.-C. Yen, and N. V. Thakor, "Wireless power delivery to flexible subcutaneous implants using capacitive coupling," *IEEE Trans. Microw. Theory Techn.*, vol. 65, no. 1, pp. 280–292, Jan. 2017.

[21] Q. Wang, W. Che, M. Mongiardo, and G. Monti, "Wireless power transfer system with high misalignment tolerance for bio-medical implants," *IEEE Trans. Circuits Syst. II, Exp. Briefs*, vol. 67, no. 12, pp. 3023–3027, Dec. 2020.

[22] B. J. DeLong, A. Kiourti, and J. L. Volakis, "A radiating near-field patch rectenna for wireless power transfer to medical implants at 2.4 GHz," *IEEE J. Electromagn., RF Microw. Med. Biol.*, vol. 2, no. 1, pp. 64–69, Mar. 2018.

[23] J. S. Ho *et al.*, "Wireless power transfer to deep-tissue microimplants," *Proc. Nat. Acad. Sci. USA*, vol. 111, no. 22, pp. 7974–7979, Jun. 2014.

[24] E. Y. Chow, C.-L. Yang, Y. Ouyang, A. L. Chlebowski, P. P. Irazoqui, and W. J. Chappell, "Wireless powering and the study of RF propagation through ocular tissue for development of implantable sensors," *IEEE Trans. Antennas Propag.*, vol. 59, no. 6, pp. 2379–2387, Jun. 2011.

[25] A. Basir and H. Yoo, "Efficient wireless power transfer system with a miniaturized quad-band implantable antenna for deep-body multi-tasking implants," *IEEE Trans. Microw. Theory Techn.*, vol. 68, no. 5, pp. 1943–1953, May 2020.

[26] S. A. A. Shah and H. Yoo, "Radiative near-field wireless power transfer to scalp-implantable biotelemetric device," *IEEE Trans. Microw. Theory Techn.*, vol. 68, no. 7, pp. 2944–2953, Jul. 2020.

[27] S. Bakogianni and S. Koulouridis, "A dual-band implantable rectenna for wireless data and power support at sub-GHz region," *IEEE Trans. Antennas Propag.*, vol. 67, no. 11, pp. 6800–6810, Nov. 2019.

[28] C. Liu, Y.-X. Guo, H. Sun, and S. Xiao, "Design and safety considerations of an implantable rectenna for far-field wireless power transfer," *IEEE Trans. Antennas Propag.*, vol. 62, no. 11, pp. 5798–5806, Nov. 2014.

[29] E. Rammos and A. Roederer, "Self-diplexing circularly polarised antenna," in *Proc. Int. Symp. Antennas Propag. Soc., Merging Technol.*, vol. 2, 1990, pp. 803–806.

[30] A. Iqbal, M. A. Selmi, L. F. Abdulrazak, O. A. Saraereh, N. K. Mallat, and A. Smida, "A compact substrate integrated waveguide cavity-backed self-triplexing antenna," *IEEE Trans. Circuits Syst. II, Exp. Briefs*, vol. 67, no. 11, pp. 2362–2366, Nov. 2020.

[31] A. Iqbal, A. Bouazizi, A. Smida, A. Basir, and U. Naeem, "Low-profile dual-band antenna with on-demand beam switching capabilities," *IET Microw., Antennas Propag.*, vol. 14, no. 1, pp. 15–20, 2019.

[32] P.-L. Chi, R. Waterhouse, and T. Itoh, "Antenna miniaturization using slow wave enhancement factor from loaded transmission line models," *IEEE Trans. Antennas Propag.*, vol. 59, no. 1, pp. 48–57, Jan. 2011.

[33] A. Iqbal, A. Smida, A. J. Alazemi, M. I. Waly, N. Khaddaj Mallat, and S. Kim, "Wideband circularly polarized MIMO antenna for high data wearable biotelemetric devices," *IEEE Access*, vol. 8, pp. 17935–17944, 2020.

[34] L. Li, H. Liu, H. Zhang, and W. Xue, "Efficient wireless power transfer system integrating with metasurface for biological applications," *IEEE Trans. Ind. Electron.*, vol. 65, no. 4, pp. 3230–3239, Apr. 2018.

[35] B. Wang, K. H. Teo, T. Nishino, W. Yerazunis, J. Barnwell, and J. Zhang, "Experiments on wireless power transfer with metamaterials," *Appl. Phys. Lett.*, vol. 98, no. 25, Jun. 2011, Art. no. 254101.

[36] S. Kim, J. S. Ho, and A. S. Y. Poon, "Midfield wireless powering of subwavelength autonomous devices," *Phys. Rev. Lett.*, vol. 110, no. 20, May 2013, Art. no. 203905.

[37] C. Song *et al.*, "A novel six-band dual CP rectenna using improved impedance matching technique for ambient RF energy harvesting," *IEEE Trans. Antennas Propag.*, vol. 64, no. 7, pp. 3160–3171, Jul. 2016.

[38] S. Mondal, D. Kumar, and P. Chahal, "A continuous-mode single-antenna harmonic RFID tag," *IEEE Microw. Wireless Compon. Lett.*, vol. 30, no. 4, pp. 441–444, Apr. 2020.

[39] H. Tafekirt, J. Pelegri-Sebastia, A. Bouajaj, and B. M. Reda, "A sensitive triple-band rectifier for energy harvesting applications," *IEEE Access*, vol. 8, pp. 73659–73664, 2020.

[40] S. K. Divakaran, D. D. Krishna, and Nasimuddin, "RF energy harvesting systems: An overview and design issues," *Int. J. RF Microw. Comput.-Aided Eng.*, vol. 29, no. 1, Jan. 2019, Art. no. e21633. [Online]. Available: https://onlinelibrary.wiley.com/doi/abs/10.1002/mmce.21633

[41] R. Das, A. Basir, and H. Yoo, "A metamaterial-coupled wireless power transfer system based on cubic high-dielectric resonators," *IEEE Trans. Ind. Electron.*, vol. 66, no. 9, pp. 7397–7406, Sep. 2019.

[42] N. D. Au, H. Le-Fuu, and C. Seo, "A wide dynamic-range rectifier at 433 MHz for multiple-antenna impedances," *IEEE Microw. Wireless Compon. Lett.*, vol. 31, no. 2, pp. 196–199, Feb. 2020.

Amjad Iqbal (Graduate Student Member, IEEE) received the B.S. degree in electrical engineering from COMSATS University, Islamabad, Pakistan, in 2016, and the M.S. degree in electrical engineering from the Department of Electrical Engineering, CECOS University of IT and Emerging Science, Peshawar, Pakistan, in 2018.

He worked as a Lab Engineer with the Department of Electrical Engineering, CECOS University Peshawar, from 2016 to 2018. His research interests include printed antennas, flexible antennas, implantable antennas, MIMO antennas, dielectric resonator antennas, wireless power transfer, and synthesis of microwave components.

Mr. Iqbal is a recipient of the Best Paper Award 2019 by IEEE AP/MTT/EMC joint chapter Malaysia.

Muath Al-Hasan (Senior Member, IEEE) received the B.A.Sc. degree in electrical engineering from the Jordan University of Science and Technology, Jordan, in 2005, the M.A.Sc. degree in wireless communications from Yarmouk University, Jordan, in 2008, and the Ph.D. degree in telecommunication engineering from the Institut National de la Recherche Scientifique (INRS), Université du Québec, QC, Canada, 2015.

From 2013 to 2014, he was with Planets Inc., CA, USA. In May 2015, he joined Concordia University, Canada, as a Post-Doctoral Fellowship. He is currently an Assistant Professor with Al Ain University, Al Ain, United Arab Emirates. His current research interests include antenna design at millimeter-wave and terahertz, channel measurements in multiple-input and multiple-output (MIMO) systems, and machine learning and artificial intelligence in antenna design.

Ismail Ben Mabrouk (Senior Member, IEEE) received the B.A.Sc. and M.A.Sc. degrees in electrical engineering from the University of Lille, Lille, France, in 2006 and 2007, respectively, and the Ph.D. degree in electrical engineering from the University of Quebec, QC, Canada, in 2012.

From 2007 to 2009 he was with Huawei Technologies, Paris, France. In 2012, he joined the Wireless Devices and Systems (WiDeS) Group, University of Southern California, Los Angeles, CA, USA. He is currently an Assistant Professor with Durham University, Durham, U.K. His research activities have been centered on implantable and wearable antenna design, propagation studies for multiple-input and multiple-output (MIMO) systems at the millimeter-wave and THz frequencies, deep learning, and wireless body area network for medical applications.

Dr. Mabrouk is a recipient of the Abu Dhabi Award for Research Excellence (AARE).

Abdul Basir (Graduate Student Member, IEEE) was born in Khyber Pakhtunkhwa, Pakistan, in 1989. He received the B.Sc. degree in telecommunication engineering from the University of Engineering and Technology, Peshawar, Pakistan, in 2015. He is currently pursuing the M.S. degree leading to the Ph.D. degree in biomedical engineering at Hanyang University, Seoul, South Korea.

His research interests include implantable antennas and systems, biomedical circuits, wearable antennas, MIMO communication, metamaterial, dielectric resonator antennas, reconfigurable antennas, long-range wireless power transfer, and wireless charging of biomedical implants.

Mr. Basir was awarded with Silver Prize for the Best Student Paper Awards in Student Paper Contests 2018 and 2019, IEEE Seoul Section. His collaborated article was awarded the Best Paper Award 2019 by IEEE AP/MTT/EMC joint chapter Malaysia. He is also awarded Third Prize for the Best Student Paper Completion 2018 by the Korea Communications Agency (KCA) and Korean Institute of Electromagnetic Engineering & Science (KIEES).

Mourad Nedil (Senior Member, IEEE) received the Dipl. Ing. degree from the University of Algiers (USTHB), Algiers, Algeria, in 1996, the D.E.A (M.S.) degree from the University of Marne la Vallée, Marne la Vallée, France, in 2000, and the Ph.D. degree from the Institut National de la Recherche Scientifique (INRS-EMT), Université de Québec, Montréal. QC, Canada, in April 2006.

He completed a Post-Doctoral Fellowship with INRS-EMT, within the RF Communications Systems Group, from 2006 to 2008. In June 2008, he joined the Engineering School Department, University of Quebec at abitibi-Témiscamingue, Val-d'Or, QC, Canada, where he is currently a Full Professor. His research interests include antennas, MIMO radio-wave propagation, and microwave devices.

Hyoungsuk Yoo (Senior Member, IEEE) received the B.Sc. degree in electrical engineering from Kyungpook National University, Daegu, South Korea, in 2003, and the M.Sc. and Ph.D. degrees in electrical engineering from the University of Minnesota, Minneapolis, MN, USA, in 2006 and 2009, respectively.

In 2009, he joined the Center for Magnetic Resonance Research, University of Minnesota, as a Post-Doctoral Associate. In 2010, he joined Cardiac Rhythm Disease Management, Medtronic, MN, USA, as a Senior EM/MRI Scientist. From 2011 to 2018, he was an Associate Professor with the Department of Biomedical Engineering, School of Electrical Engineering, University of Ulsan, Ulsan, South Korea. Since 2018, he has been an Associate Professor with the Department of Biomedical Engineering, Hanyang University, Seoul, South Korea. He has been the CEO of E2MR, a startup company, since 2017. His current research interests include electromagnetic theory, numerical methods in electromagnetics, metamaterials, antennas, implantable devices, and magnetic resonance imaging in high-magnetic field systems.

Dr. Yoo was awarded Third Prize for the Best Student Paper at the 2010 IEEE Microwave Theory and Techniques Society International Microwave Symposium.